Additive Manufacturing 38 (2021) 101833

Contents lists available at ScienceDirect

Additive Manufacturing

journal homepage: www.elsevier.com/locate/addma

Research Paper

# Modeling of porosity and grain size effects on mechanical behavior of additively manufactured structures

Mehdi Hamid [a,1,*], M. Sadeq Saleh [b], Ali Afrouzian [a], Rahul Panat [b,*], Hussein M. Zbib [a]

[a] School of Mechanical and Materials Engineering, Washington State University, Pullman, WA 99164, United States
[b] Department of Mechanical Engineering, Carnegie Mellon University, Pittsburgh, PA 15213, United States

ARTICLE INFO

**Dedication:** This paper is dedicated to the loving memory of Prof. Hussein Zbib (1958–2020), a mentor, colleague, and friend, who passed away during the course of this investigation.

*Keywords:*
Additive manufacturing
Mechanical behavior of AM structures
Continuum mechanics
Strain gradient plasticity
Grain size
Dislocation dynamics
Finite element analysis (FEA)

ABSTRACT

Additive manufacturing (AM) methods such as Aerosol Jet (AJ) printing allow the fabrication of structures via sintering of micro and/or nanoparticles, leading to microstructures that consist of various combinations of pore and grain sizes. It has been reported that AJ printed and sintered silver micropillars show an unusual behavior of high stiffness and high strain-to-failure for structures with high porosity and vice versa (Saleh et al. 2018 [1]). This behavior, however, is accompanied by the stiffer structures having smaller grain sizes and softer structures having larger grain sizes. To explain the physics of this behavior where a trade-off between hardening caused by size effects (grain refinement and gradients) and softening caused by porosity is expected to play a critical role, a multi-scale modeling approach is proposed in this paper. The model formulation consists of a continuum dislocation dynamics (CDD) framework, coupled with continuum plasticity and finite element analysis. The dislocation dynamics formulation is introduced into a user material subroutine and coupled with a finite element commercial solver, in this case, LS-DYNA, to solve the model in three-dimensional scale with the same size as the AM micropillars. The results from the model capture the general trends observed in compression tests of AM micropillars. In particular, it is shown that the grain size and dislocation density have a disproportionately higher influence over the mechanical deformation of metallic structures when compared to the porosity. These results show that the behavior of AM structures in the plastic regime is dominated by grain size effects rather than porosity. Some limitations of the model and possible future refinements are discussed. The paper provides an important analytical framework to model the mechanical behavior of AM structures with internal porosity in the plastic regime.

## 1. Introduction

Additive manufacturing (AM) has allowed the fabrication of metallic parts having complex architectures, unique material combinations, and controlled microstructures [2]. The AM of metal part involves sintering and/or melting-solidification of micro or nanoparticles, which often leads to an internal part porosity [3]. In fact, the porosity and other defects are common to parts fabricated by AM [4]. Further, the AM methods allow the control of the grain size via changes to the starting powders and the process parameters. In addition, the microstructures of parts made by AM are complex [5], which can give rise to local stress and strain gradients that can affect their mechanical performance. The mechanical behavior of AM parts is thus expected to be an interplay between the defects such as internal porosity, the grain size/distribution, and their evolution during deformation.

Aerosol Jet (AJ) nanoparticle printing is an AM method that can be used to fabricate three-dimensional microscale structures. Such structures can be used as electrodes for high-capacity Li-ion batteries [6] where typical forces on the structures during lithiation and delithiation cycles can be of the order of tens of MPa [7]. In our previous work [1], AJ nanoparticle printing was used to create 3D micropillars of pure polycrystalline silver having a diameter of 80–90 μm and a height of about 900 μm. Different average grain sizes - between 250 nm and 5 μm - were obtained by sintering of the micropillars at four different temperatures of 250 °C, 350 °C, 450 °C, and 550 °C. The sintering conditions also produced porosities in the range of 20–0%, respectively [1]. The complexity of AJ printed, and sintered microstructures is demonstrated in Fig. 1a–c. The micropillars in Fig. 1a are fabricated using

* Corresponding authors.
*E-mail addresses:* mehdi.hamid@wsu.edu (M. Hamid), rpanat@andrew.cmu.edu (R. Panat).
[1] IBM Systems, 3605 Highway 52 North, Rochester, MN 55901, United States.

https://doi.org/10.1016/j.addma.2020.101833
Received 17 August 2020; Received in revised form 28 December 2020; Accepted 29 December 2020
Available online 5 January 2021

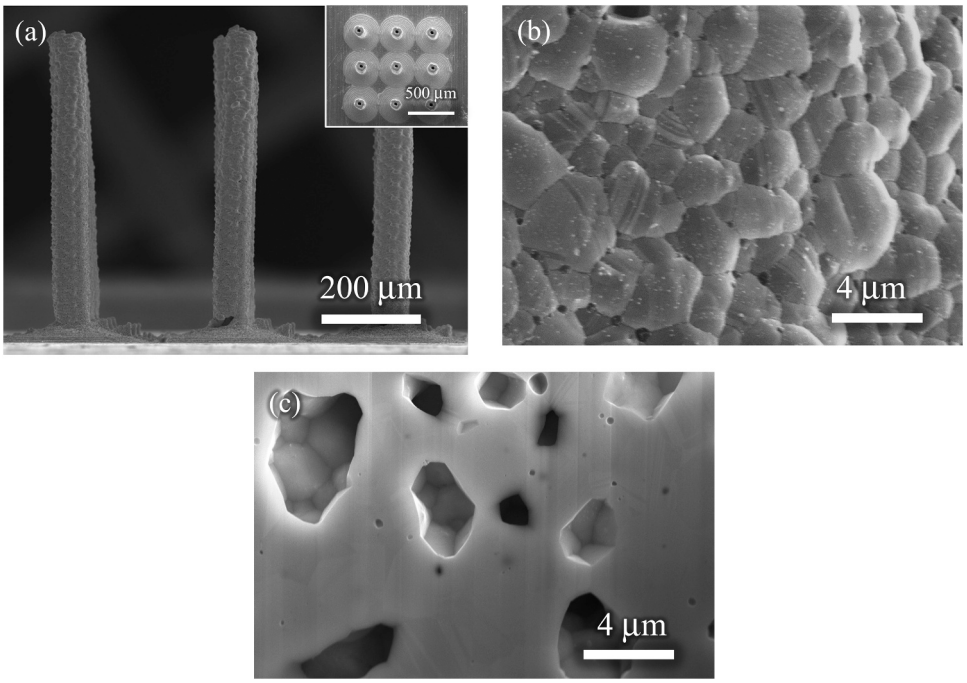


**Fig. 1.** Complex microstructures created by Aerosol Jet nanoparticle printing process. (a, b) Scanning electron microscope (SEM) images of additively manufactured 3 × 3 silver micropillar array showing a microstructure consisting of grains that are 2–4 μm in size. (c) Cross-section of a micropillar made by focused ion beam (FIB) showing internal porosity due to particle sintering.

nanoparticles with 50–150 nm size, which after sintering, resulted in the microstructures shown in Fig. 1b and c. It is clear from Fig. 1 that the AM microstructures tend to be complex in nature, consisting of internal porosity with pores having irregular sizes and shapes, and a characteristic grain size distribution that arises from sintering and growth of the printed nanoparticles (also see Ref. [8]). In addition, these microstructures are expected to give rise to local stress and strain gradients that can affect their global deformation. The AM micropillars (e.g. similar to that shown in Fig. 1) were subjected to compressive loads by Saleh et al. [1], which showed an unusual behavior consisting of an increase in effective modulus and decrease in strain-to-failure with increasing porosity. This was, however, accompanied by a decrease in grain size. In other words, the mechanical behavior of the AM micropillars could be attributed to two competing mechanisms, namely, strengthening arising from strain gradients [9] and grain size effect [10], and softening arising from degradation of strength caused by porosity. Although a semi-empirical two-phase model [11] was used to qualitatively explain these trends, a multi-scale modeling approach is needed to explain the physics of deformation of AM structures that takes into account the physical processes occurring at microscale (dislocations density effects) and at macroscale (global strain and stress, size effects, porosity).

There have been a few modeling efforts that take into account the multiscale features observed in AM structures [12]. A 2D crystal plasticity-based model was developed for structures of 316 stainless steel fabricated by Selective Laser Melting (SLM) to capture the role of texture, process defects, mechanical loading direction, and laser hatch space [13]. In this work [13], a Voronoi tessellation method was applied to create different microstructures to analyze the effect of spatial grain distribution on the mechanical properties of SLM printed samples. A crystal plasticity model was developed for single crystal metallic samples with voids and was interfaced with a finite element solver to analyze the effect of stress triaxiality, initial porosity, crystal orientation, void growth, and coalescence [14]. None of the prior models take into account the interplay between porosity and grain sizes created by particle coalescence in AM structures in a three-dimensional stress-state.

The CDD theory consists of a novel constitutive law, based on dislocation density evolution mechanisms coupled with continuum plasticity, and is able to predict phenomenological representation of dislocation evolution, production, and annihilation within the samples under stress. The benefit of this method over conventional continuum mechanics is that it allows the implementation of small-scale parameters associated with Burger's vector, grain size, and grain boundary that are physical properties of the materials. These parameters cannot be incorporated in a conventional continuum mechanics formulation. Incorporation of these parameters improves the accuracy of prediction of deformation of a part in the plastic regime [15–18].

The impetus for the present work is thus twofold. First, we aimed to create a realistic modeling framework to capture the deformation of AM parts that takes into account the multi-scale microstructural features arising from the additive processes. These features include a combination of grain sizes, porosities, dislocations densities, and shape imperfections resulting from different processing conditions. Continuum dislocation dynamics (CDD) model developed earlier by the authors (Aksari et al. [19] and Li et al. [15]) is coupled with continuum plasticity and finite element method to capture the interaction of grain sizes, porosity, stress-strain gradients, and sample length scales observed in experiments [1] during deformation. The porosity is incorporated via a viscoplasticity model, which is coupled with the CDD framework. Second, we aimed to use this modeling framework to capture the physics of the mechanical behavior of AJ printed metallic micropillars [1] under compressive stress. The focus of this part was to employ a stress-strain gradient theory which combined a stress-gradient theory [20–22], with a strain-gradient theory [17,23–25] into the CDD framework in order to analyze the grain size and porosity effects for the microstructures and length scales observed in the AM micropillar to explain the results from Saleh et al. [1].

We note that one of the novelties of this work lies in coupling of the continuum mechanics-based FEA solver (LS-DYNA) with a CDD-based viscoplastic formulation. For example, in continuum mechanics, length scale parameters like grain size and porosity do not exist. By applying the CDD viscoplastic formulation, grain size, porosity, initial dislocation density, and its evolution are implemented in the study. It

should be noted that all these parameters can be experimentally measured, so the coupled model has the advantage of taking physical inputs based on material properties and the work hardening history, which is not the case for any other commercial continuum mechanics-based FEA solvers such as Ansys and Abaqus. This capability is of significant importance for AM samples, since they typically undergo some level of post-processing and heat treatment prior to usage in the field.

We first introduce the continuum mechanics formulation which incorporates the effect of porosity. The dislocation dynamics formulation and its coupling with the continuum model are then discussed. The coupled model is introduced into a finite element framework for a simple tensile model and test verification. The modeling predictions of tensile stress vs strain curve for various initial dislocation densities are compared with the experimental data from literature [21] to determine the optimum value for initial dislocation density. Finally, the FEM simulation results for micropillars are presented, discussed, and compared to experimental results.

## 2. Viscoplasticity-porosity model coupled with continuum dislocation dynamics

In order to model the AM fabricated metallic structures, a viscoplasticity-porosity model is developed and coupled with the CDD model, which is implemented into a finite element framework. The finite element method is used to investigate the deformation of the micropillars for various grain sizes and porosities. The geometry of the micropillars is designed in LS-PrePost [26] using dimensions of the 3D printed structures [21]. A set of plasticity equations are implemented into a user material subroutine based on dislocation density interaction mechanisms and stress/strain gradient theories. The simulations are performed with LS-DYNA and a user material subroutine (UMAT) is written in Fortran environment. Also, in order to compute spatial gradients, a Matlab-based code is developed which identifies the surrounding neighbors for each solid element. The output of the Matlab code is read by UMAT which is used for finding neighboring elements in the stress and strain gradient calculations. The plasticity model is compared to tensile test results with available experimental data for 99.9% pure silver from literature. Next, a 3D model with solid elements is designed with the same geometry of additively manufactured micropillars, and a parametric study is carried out to investigate the influence of microstructural and material parameters.

### 2.1. Viscoplasticity-porosity model

To develop the viscoplasticity-porosity model, we first note that in continuum mechanics framework, the velocity gradient tensor, $\boldsymbol{L}$, is decomposed into a symmetric part, $\boldsymbol{D}$, and an antisymmetric part, $\boldsymbol{W}$, as [27],

$$\boldsymbol{L} = \boldsymbol{D} + \boldsymbol{W} \tag{1}$$

with $\boldsymbol{D}$ being the strain rate tensor, and $\boldsymbol{W}$ being the spin tensor given by,

$$\boldsymbol{D} = \frac{1}{2}[\boldsymbol{L} + \boldsymbol{L}^T] \tag{2}$$

$$\boldsymbol{W} = \frac{1}{2}[\boldsymbol{L} - \boldsymbol{L}^T] \tag{3}$$

The strain rate tensor, $\boldsymbol{D}$, is further decomposed as the sum of elastic ($\boldsymbol{D}^e$) and plastic ($\boldsymbol{D}^p$) terms such that,

$$\boldsymbol{D} = \boldsymbol{D}^e + \boldsymbol{D}^p \tag{4}$$

Assuming linear elastic isotropic material with isotropic damage due to porosity, Hooke's law is given by the following relation [28],

$$\hat{\boldsymbol{\sigma}} = (1 - \varnothing)[\boldsymbol{C}^e]\boldsymbol{D}^e \tag{5}$$

where $[\boldsymbol{C}^e]$ is the fourth order elasticity tensor, $\hat{\boldsymbol{\sigma}}$ is co-rotational rate of the Cauchy stress tensor, $\boldsymbol{\sigma}$, and $\varnothing$ is the porosity. Note that the growth of microvoids (and hence porosity $\varnothing$) plays a significant role during the process of plastic deformation in crystal plasticity of metals during nonlinear deformation. In our calculations, we are assuming that the voids are uniformly distributed and will update the Cauchy stress. Furthermore, for isotropic plastic deformation with isotropic porosity, we assume a plastic potential of the form $f = J_2 + \phi I_1^2$ [29,30], where $J_2 = \frac{1}{2}\boldsymbol{S}:\boldsymbol{S}$ is the second invariant of the deviatoric stress $\boldsymbol{S} = \boldsymbol{\sigma} - (tr\boldsymbol{\sigma}/3)\boldsymbol{I}$, with $\boldsymbol{I}$ being the unit tensor, and $I_1 = tr\boldsymbol{\sigma}$ being the first stress invariant. Then, with the associated rule of plastic flow being normal to the plastic potential, we obtain the following for the plastic strain rate tensor $\boldsymbol{D}^P$,

$$\boldsymbol{D}^p = \frac{\dot{\bar{\gamma}}^p}{2\bar{\tau}} \quad [\boldsymbol{S} + (2\phi I_1)\boldsymbol{I}] \tag{6}$$

$$\dot{\bar{\gamma}}^p = \quad \sqrt{2\boldsymbol{D}^p:\boldsymbol{D}^p} \tag{7}$$

$$\bar{\tau} = \sqrt{J_2 + 6(\phi I_1)^2} \tag{8}$$

with $\bar{\tau}$ being the effective shear stress for the material with porosity, and $\dot{\bar{\gamma}}^p$ being the effective plastic shear strain rate. As can be inferred from Eq. (6), the very existence of porosity implies a finite volumetric plastic deformation rate. In this paper, we consider relatively small strains, and assume a constant porosity throughout the deformation process. However, for later stages of deformation, an evolution law for the porosity can be introduced [30].

Analogous to the dislocation-based crystal plasticity framework [15], the effective plastic shear strain rate $\dot{\bar{\gamma}}^p$ is determined through the Orowan relation [31] as,

$$\dot{\bar{\gamma}}^p = \rho_M b \bar{v}_g, \tag{9}$$

where $\rho_M$ is the density of mobile dislocations, $b$ is the magnitude of the Burgers vector, and $\bar{v}_g$ is the average dislocation glide velocity. In turn, we assume a power law for the dislocation velocity and introduce the effect of porosity as a softening mechanism in the expression for the critical shear stress [15]:

$$\bar{v}_g = v_0 \left( \frac{\bar{\tau}}{\tau_{cr}^*} \right)^{1/m} \quad , \quad \tau_{cr}^* = \quad \tau_{cr}(1 - \phi^n), \tag{10}$$

where $\tau_{cr}$ is the critical shear stress, $m$ is strain rate sensitivity, and $v_0$ is reference velocity [19]. The effective yield shear stress, $\tau_{cr}^*$, defined above, accounts for softening resulting from the porosity. The value for the power $n$ depends upon the assumed shape of the void (e.g. $n = 1/2$ for cylindrical voids [30]). In this work, for consistency with the assumption of isotropic damage model, we assume $n = 1$. The matrix material (surrounding the spherical voids, $n = 1$) is also assumed to be isotropic that obeys the von Mises flow rule according to the $J_2$ theory of plasticity. The yield function for the voided material is then obtained by modifying the $J_2$ yield function by adding a hydrostatic term [32]. Also, ductile damage is usually approached by using isotropic damage models in which voids are assumed to be spherical while the matrix material is assumed to be isotropic [33]. In the above formulation, porosity decreases the overall elastic stiffness, load carrying capacity of the material, and the local critical shear stress for plastic shearing; and can be deduced from Eqs. (5), (8) and (10).

### 2.2. Coupling of viscoplasticity-porosity model with continuum dislocation dynamics

In the viscoplasticity-porosity formulation, there are two internal state variables, in addition to porosity, that depend on the microstructure, namely, the dislocation density and the critical shear stress.

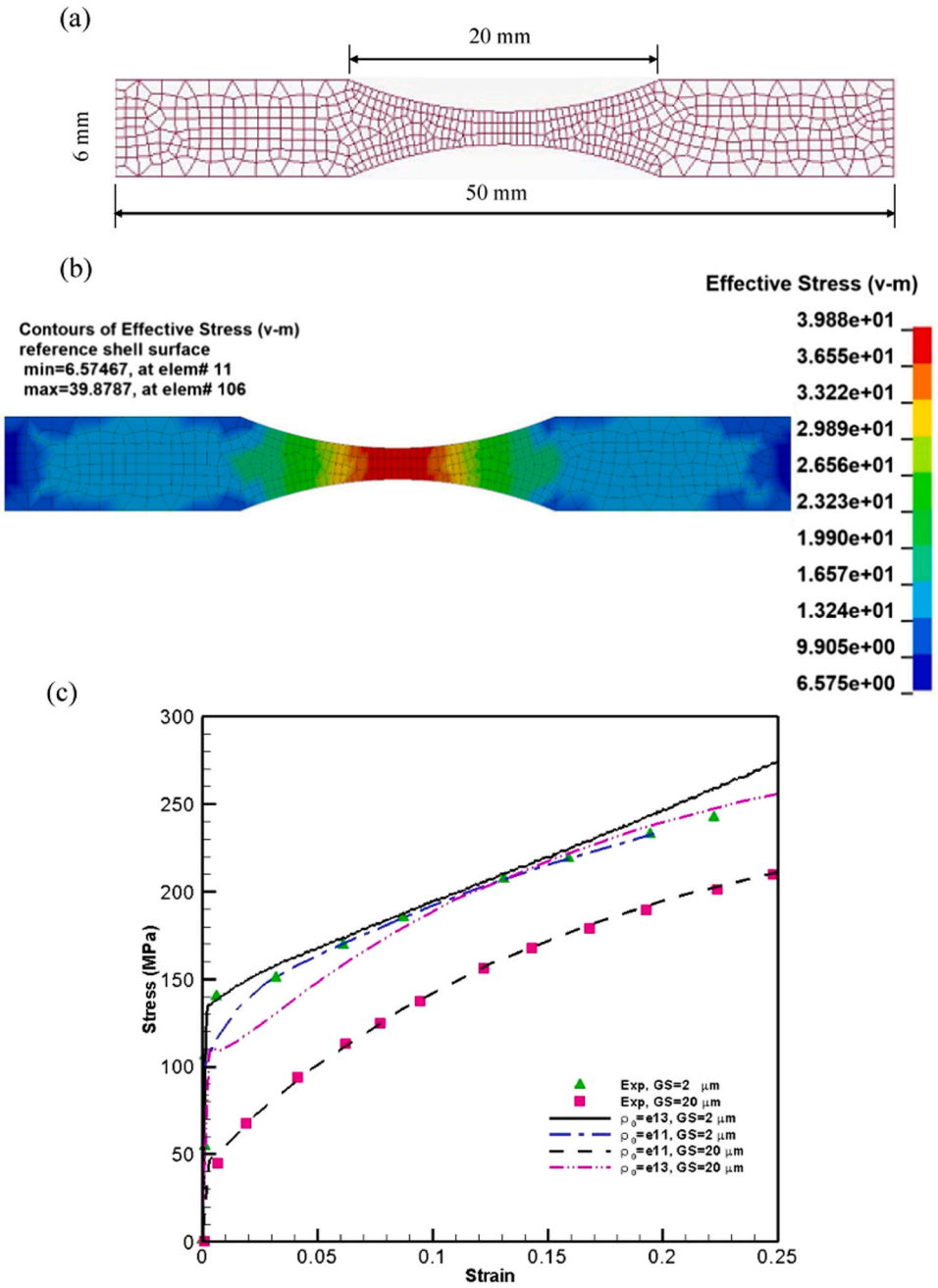


**Fig. 2.** (a) Dog-bone shaped tensile test specimen for modeling, (b) contour of effective stress (units in MPa), and (c) numerical stress-strain curves and comparison with experiments [21] (Exp: experiment, GS: Grain size, $\rho_0$: Initial dislocation density).

Assuming one internal variable to describe the dislocation density, the rate equation of the dislocation density was derived by Kocks [34] and consists of two terms - production and annihilation. Here, we assume that the total statistically stored dislocation density can be written as the sum of mobile dislocation density $\rho_M$ and immobile dislocation density $\rho_I$,

$$\rho_T = \rho_M + \rho_I \tag{11}$$

This way, only the mobile dislocation density contributes to plastic shearing via Eq. (9), while the sum of the mobile and immobile dislocations contributes to strain hardening by the Bailey-Hirsch relation. The evolution equations for the mobile and immobile dislocation densities, derived in [15], are as follows:

$$\dot{\rho}_M = (\beta_1 - \beta_3)\rho_M - \beta_2\rho_M^2 + \beta_4\rho_I - \beta_5\rho_I\rho_M \tag{12}$$

$$\dot{\rho}_I = \beta_3\rho_M - \beta_4\rho_I - \beta_5\rho_I\rho_M \tag{13}$$

where $\beta_1 = \alpha_1\frac{\bar{v}_g}{\bar{l}_g}$, $\beta_2 = 2\alpha_2 R_c\bar{v}_g$, $\beta_3 = \alpha_3\frac{\bar{v}_g}{\bar{l}_g}$, $\beta_4 = \alpha_4\frac{\bar{v}_g}{\bar{l}_g}\left|\frac{\bar{\tau}}{\tau_{cr}}\right|^r$, $\beta_5 = \alpha_5 R_c\bar{v}_g$,

**Table 1**
Description of mechanisms and parameters.

| Parameters | Mechanisms |
|---|---|
| $\alpha_1$ | Multiplication of dislocations from sources |
| $\alpha_2$ | Mobile-mobile dislocation annihilation |
| $\alpha_3$ | Locking of mobile dislocations |
| $\alpha_4$ | Unlocking of immobile dislocations |
| $\alpha_5$ | Mobile-immobile annihilation |

**Table 2**
Material properties for silver applied in the CDD framework.

| | |
|---|---|
| Young's modulus (E) [40,41] | 78 GPa |
| Poisson's ratio ($\vartheta$) [42] | 0.37 |
| Shear modulus (μ) | 28.5 GPa |
| Friction stress ($\tau_0$) [43] | 11 MPa |
| Burgers vector magnitude (B) [44] | 0.288 nm |
| Reference velocity ($v_0$) [45] | $10^{-5}$ $ms^{-1}$ |
| Bailey-Hirsch parameter ($\alpha^*$) [17] | 0.1 |
| Hall-Petch coefficient (K) [43] | 4.2 MPa $mm^{1/2}$ |
| $\alpha_1, \alpha_2, \alpha_3, \alpha_4, \alpha_5$ | 0.08, 0.65, 0.002, 0.002, 1.0 |

with $\bar{l}_g$ being the dislocation mean-free path which has an inverse square root relationship with the sum of the geometrical and total dislocation densities as given in Eq. (17) of the next section. Also, $R_c$ is the capture radius for the interaction between two dislocations, and r is a numerical constant, which are set at 15b and 0.5, respectively, based on curve fit in Fig. 2 (discussed in the next section). In the equations above, there are 5 terms which represent specific dislocation interaction mechanisms. For single crystals, the parameters $\alpha_1$ to $\alpha_5$ may be calculated from smaller scale modeling of discrete dislocation dynamics and then adjusted to polycrystals by experimental curve fitting [15,19]. Table 1 explains the mechanism corresponding to each of these parameters. For the sake of brevity, the details of these 5 parameters are not explained here and the readers are referred to previous publications on this topic [15–17,19]. For example, $\alpha_1$ to $\alpha_5$ have been selected based on reference [17]. The evolution Eqs. (12) and (13) are nonlinear and coupled with strong interactions between the mobile and immobile dislocations.

The critical shear stress $\tau_{cr}$ appearing in Eq. (10) is the sum of reference shear stress $\tau_0$, forest dislocation hardening $\tau_H$, and stress-gradient dependent term $\tau_s$ [15,19], i.e.,

$$\tau_{cr} = \tau_0 + \tau_H + \tau_s \tag{14}$$

The forest dislocation hardening term $\tau_H$ is determined by the classical Bailey-Hirsch relation [35],

$$\tau_H = \alpha^* b \mu \sqrt{\rho_T} \tag{15}$$

where the parameters $\alpha^*$ and $\mu$ are Bailey-Hirsch parameter and elastic shear modulus, respectively, and shown in Table 2.

### 2.3. Size effect and gradient-dependent hardening

In the continuum dislocation dynamics framework, size effects arise from two mechanisms: geometrically necessary dislocations (GNDs), $\rho_{GND}$, and dislocation pile-ups under heterogeneous state of stress. In a rigorous treatment, the geometrically necessary dislocations can be directly related to the dislocation density Nye's tensor [36,37]. Here we adopt the following scalar form developed in [23,38],

$$\rho_{\mathrm{GND}} = \frac{1}{b}|\nabla \bar{\gamma}^p| \tag{16}$$

with $\bar{\gamma}^p$ being the effective plastic shear strain. The effect of the GNDs is incorporated into the model through the expression for the dislocation mean free path appearing in Eqs. (12) and (13), i.e.,

$$\bar{l}_g = \frac{1}{\sqrt{\rho_T + \rho_{GND}}} \tag{17}$$

By introducing the GNDs in the mean-free path, they act as barriers to mobile dislocations. Their trapping effect will accelerate the production of statistically stored dislocations where strain gradients are present, which then leads to an increase in dislocation density.

As discussed in [20,21], the mechanism of dislocation pile-ups under a heterogenous state of stress results in a stress- gradient dependent term

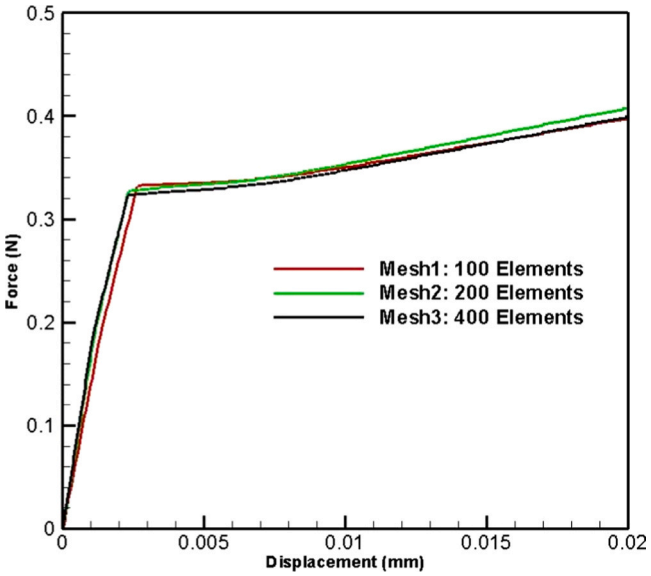


**Fig. 4.** Effect of mesh density on force-displacement curve.

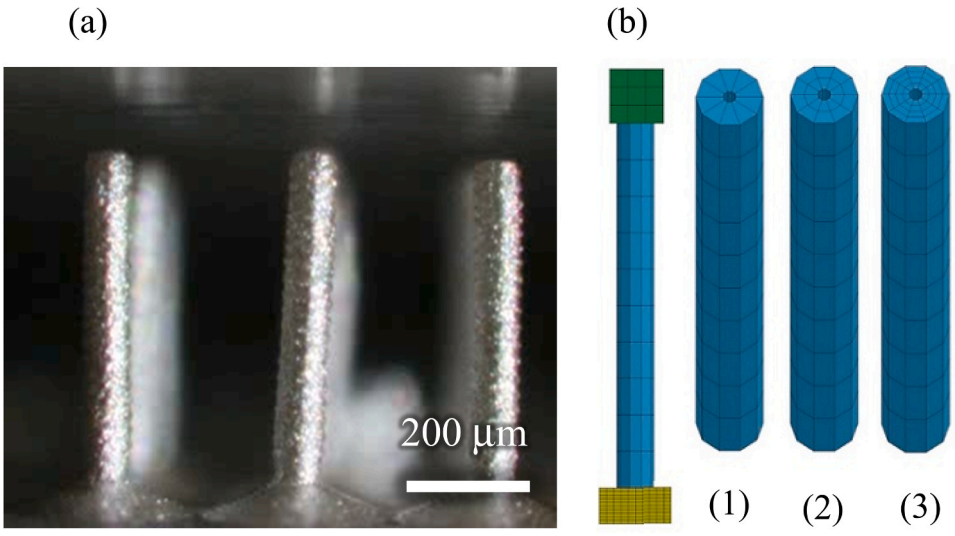


**Fig. 3.** (a) As-manufactured micropillars, and (b) model of micropillar with loading plates, and different mesh designs (Mesh1-Mesh3).

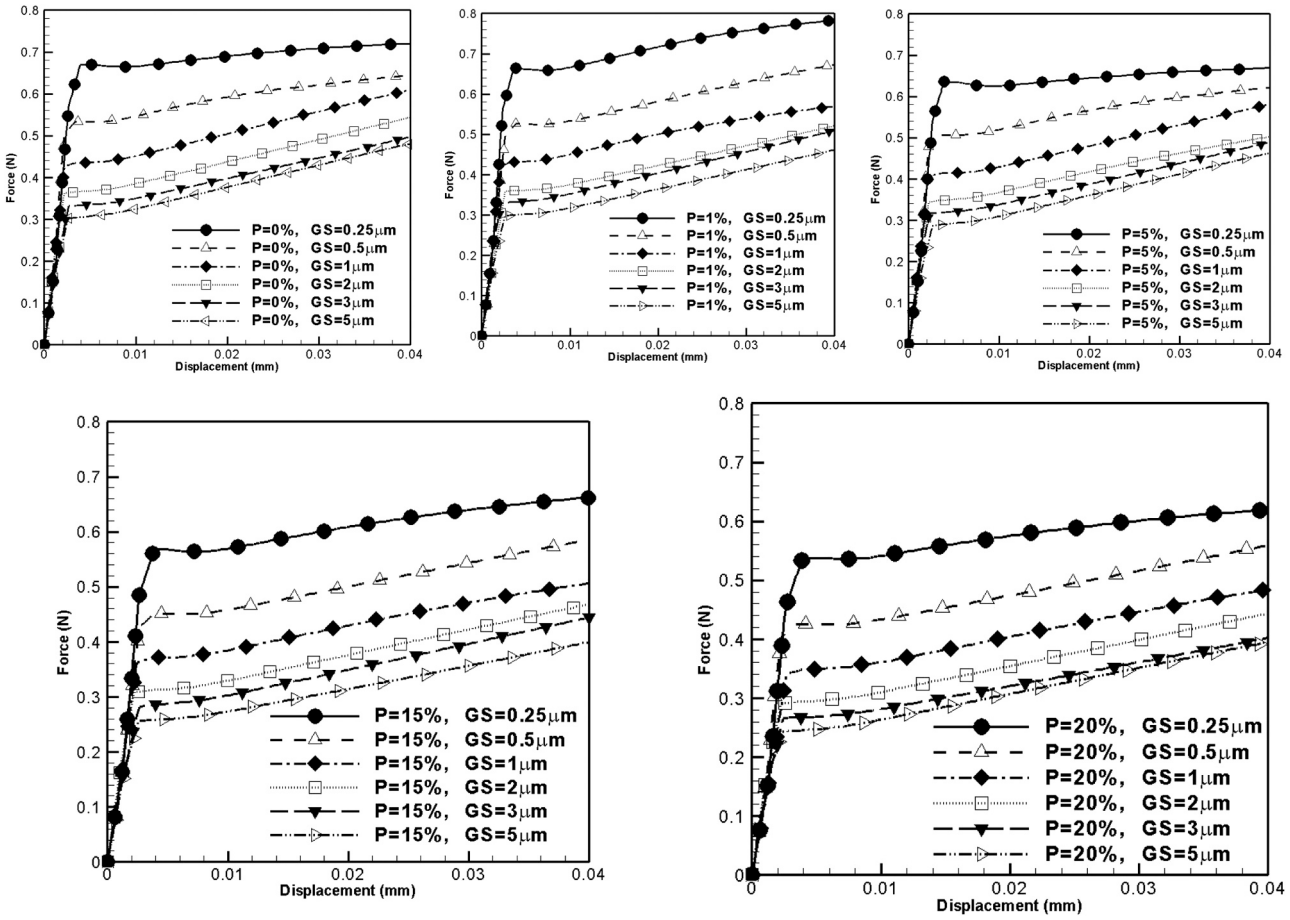


**Fig. 5.** Force-displacement curves for various porosities and grain sizes (GS).

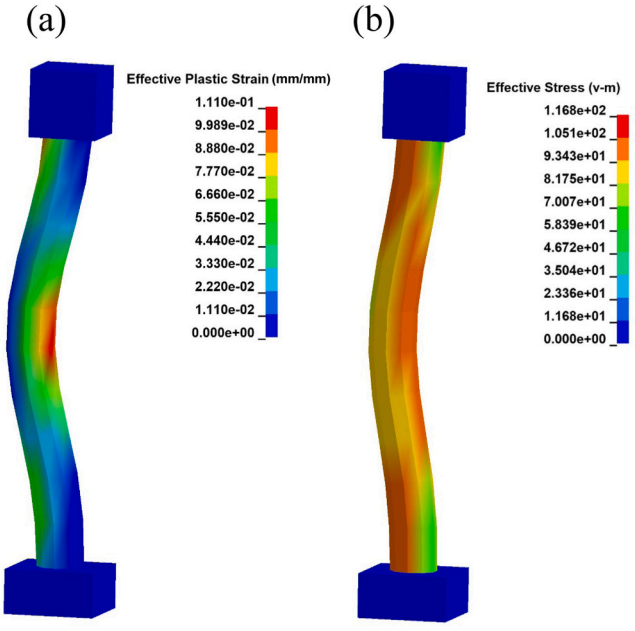


**Fig. 6.** Deformed configurations with contour plots: (a) effective plastic strain (mm/mm), and (b) effective stress in units of MPa, for 3 μm grain size with 1% porosity.

$\tau_s$, given by the following expression,

$$\tau_s = \frac{K}{\sqrt{L}}\left(1 + \frac{L'}{4\overline{\tau}}|\nabla\overline{\tau}|\right) \tag{18}$$

Here $L$ and $L'$ are length scales representing the average grain size and the obstacle (dislocation pile-ups) spacing respectively. The gradient of effective shear stress is represented by $|\nabla\overline{\tau}|$. Also, $K$ is the Hall-Petch numerical coefficient. The theory is implemented into the CDD framework and was shown to predict size effects in various microstructures [16].

The above equations are implemented into a user material subroutine in LS-DYNA to model the mechanical behavior of the polycrystalline silver micropillars. The LS-DYNA material card *MAT_USER_DEFINED_MATERIAL_MODELS [39] is used for this modeling purpose. Numerical calculation of the stress and strain gradient terms required a special treatment, which also turned out to be computationally intensive. We developed a Matlab-based code, external to LSDYNA, which identifies the surrounding neighbors for each solid mesh element. Each element is defined by an ID number and the Matlab code uses the node numbers of solid elements as an input to find neighboring elements. If any two elements share a node then the elements are counted as neighboring elements. The output of the Matlab code is then read by UMAT which is used for stress and strain gradient calculation using the central difference method. By implementing the above system of equations into a UMAT subroutine, physical parameters, like porosity, mobile and immobile dislocation densities, dislocation glide velocity, and other microstructural parameters can be directly related to plastic deformation of micropillars.

We note that in Table 2, the shear modulus was calculated based on

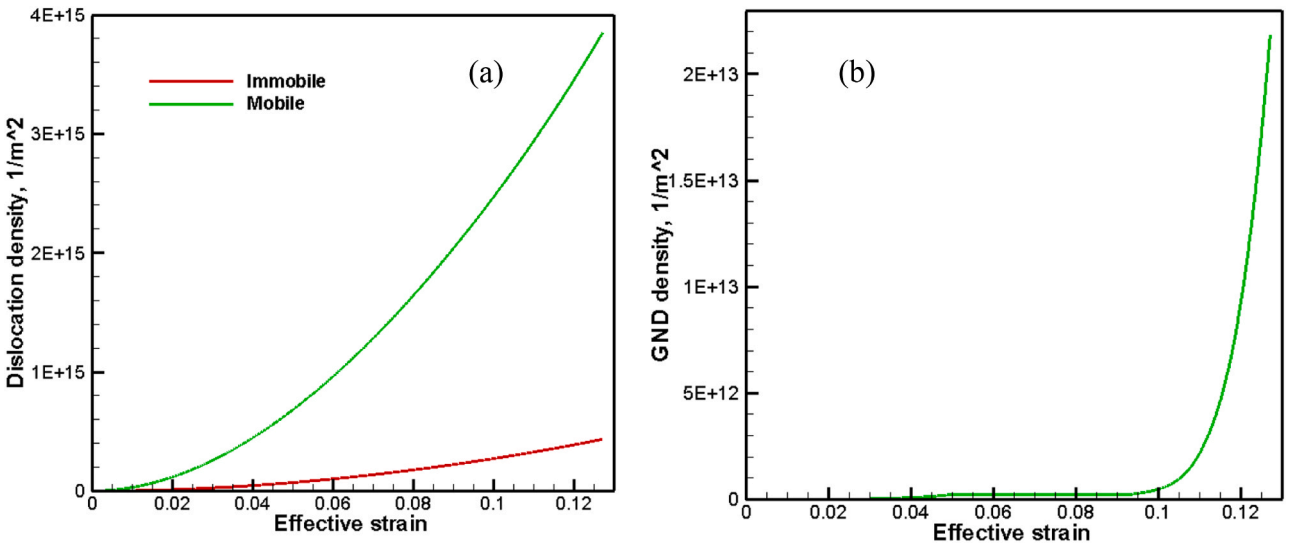


**Fig. 7.** (a) Mobile and immobile dislocation densities and (b) GND density as a function of strain at the center of the pillar, for 3 μm with 1% porosity.

the Young's modulus and Poisson ratio. The values for the parameters $\alpha_3$, $\alpha_4$,$\alpha_5$ are the same used in [17], while the values for $\alpha_1 = 0.08$ and $\alpha_2 = 0.65$ are determined by fitting to the experimental data discussed in the next section. The strain rate sensitivity, *m,* depends on the microstructure, grain size, temperature, and strain rate [46]. For pure silver, the reported values for *m* fall in the range of 0.007–0.05, depending on the strain rate and porosity percentage [47].

## 3. Preliminary numerical results and discussion

### 3.1. Model validation

We validated the model implemented in UMAT by comparing the numerical results from the model with available experimental tension test data for pure silver from the literature [48] for grain sizes of 20 μm and 2 μm. The specimen with dimensions is shown in Fig. 2a. The thickness of the specimen was 2 mm. Shell elements were used for the simulations. One end of the specimen was fixed, and the other end was subjected to a constant cross head speed of 0.05 mm/s. Fig. 2b shows a contour plot of the effective stress, which illustrates the uniformity of the stress field in the gauge (middle) section. In this simulation, we examined the effect of the initial mobile and immobile dislocation density and grain size on the stress-strain curve.

The stress-strain behavior predicted by the model is shown in Fig. 2. Also plotted in the figure is experimental data from Al-Fadhalah et al. [48] for samples with grain sizes of 20 μm and 2 μm. The results for initial dislocation density of $10^{11}$ $m^{-2}$ and $10^{13}$ $m^{-2}$ with strain rate sensitivity of 0.05 are shown. With these conditions, the predicted stress-strain behavior fits the experimental data for the case of 20 μm grain size with dislocation density of $10^{13}$ $m^{-2}$ very well. When the grain size is decreased to 2 μm, while keeping all the parameters fixed, the predicted stress-strain curve is also in good agreement with the experimental data, showing strong size effect, except for the initial part of the curve. This can be attributed to the different initial dislocation content in the fine-grained specimen [48]. By increasing the initial dislocation density to $10^{13}$ $m^{-2}$, the initial yield stress increases due to the Bailey-Hirsch effect, and the curves saturate towards the same stress levels as the plastic strain is increased. These simulations show the

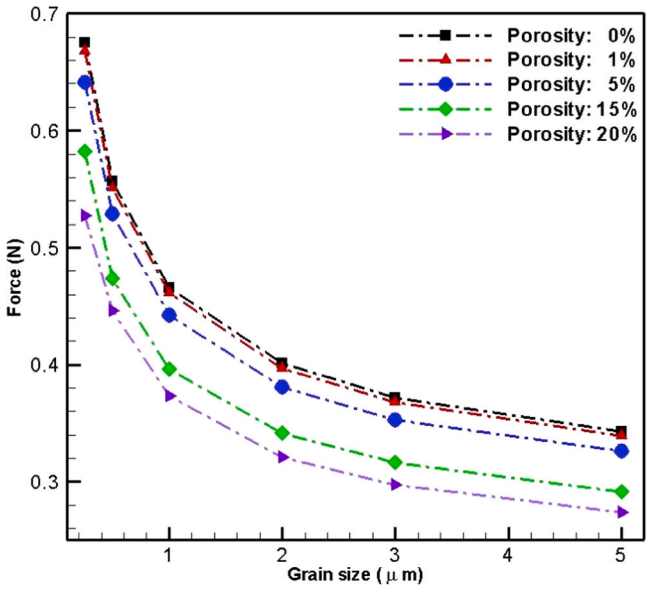


**Fig. 8.** Force at the onset of buckling versus grain size for micropillars with different porosities.

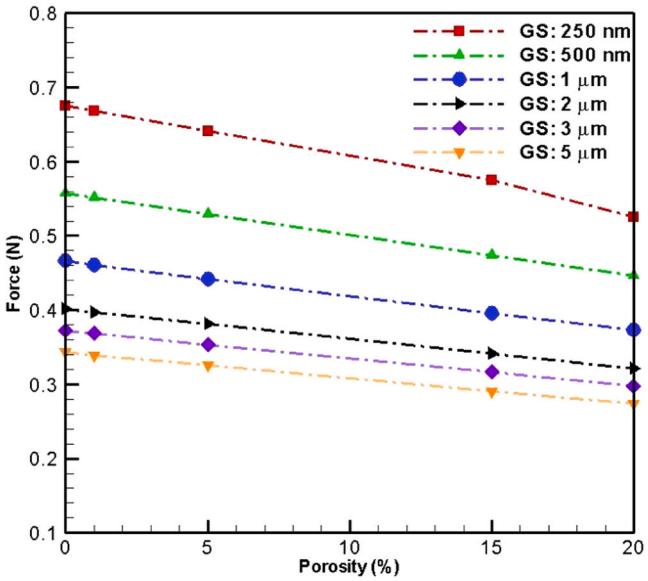


**Fig. 9.** Force at the onset of buckling versus porosity for micropillars with different grain sizes (GS).

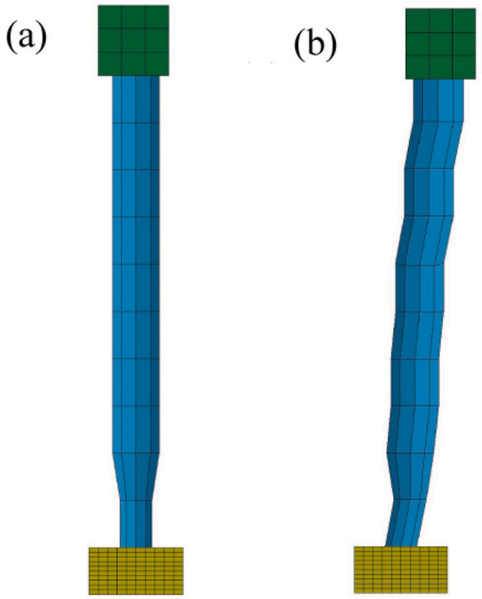


**Fig. 10.** Micropillars with imperfections. (a) A micropillar with reduced diameter at the bottom (case-II), and (b) A micropillar with reduced diameter at the bottom and a tilt with respect to the vertical axis (case-III).

interaction between dislocation content and size effects as captured by the CDD model.

### 3.2. Micropillars under compression

In this section, results are presented for micropillars that are modeled to mimic the manufactured micropillars shown in Fig. 3a (also see Fig. 1a). The geometry of the modeled micropillar is shown in Fig. 3b.

The model consists of a micropillar that is tied to a bottom rigid plate and a rigid top plate that is in sliding contact with the top surface of the micropillar. This way, while the bottom surface of the micropillar is fixed in all its degrees of freedom, the upper surface of the pillar is free to move as it is pushed down by the top rigid box. Note that in experiments in Saleh et al. [1], the pillars are firmly anchored to the substrate by printing of a larger thin circular disk near the bottom of each pillar as seen in the inset in Fig. 1a. The deformation of a single micropillar is illustrated in Supporting Information, Fig. S1, where the boundary conditions (fixed bottom surface and an upper surface that is free to move as it is pushed down) are apparent. The top rigid box is constrained to move down in the vertical direction with velocity of $2.5 \times 10^{-2}$ mm/s and is modeled as rigid body in the LS-DYNA model. The contacts between moving and fixed rigid boxes and micropillar are "automatic surface-to-surface" and "tied node-to-surface", respectively.

The micropillar is a hollow cylinder with a length of 1000 μm, inside diameter of 20 μm, and outside diameter of 90 μm. These slender cylinders are designed with eight-node brick elements. The computations turned out to be computationally intensive due to the calculations of the stress and strain gradient terms that appear in Eqs. (16) and (18). For various mesh densities, mesh1-mesh3, shown in Fig. 3b, the results in Fig. 4 shows an insignificant mesh dependency. The applied grain size for this mesh sensitivity study was 3 μm and with 0% porosity. The

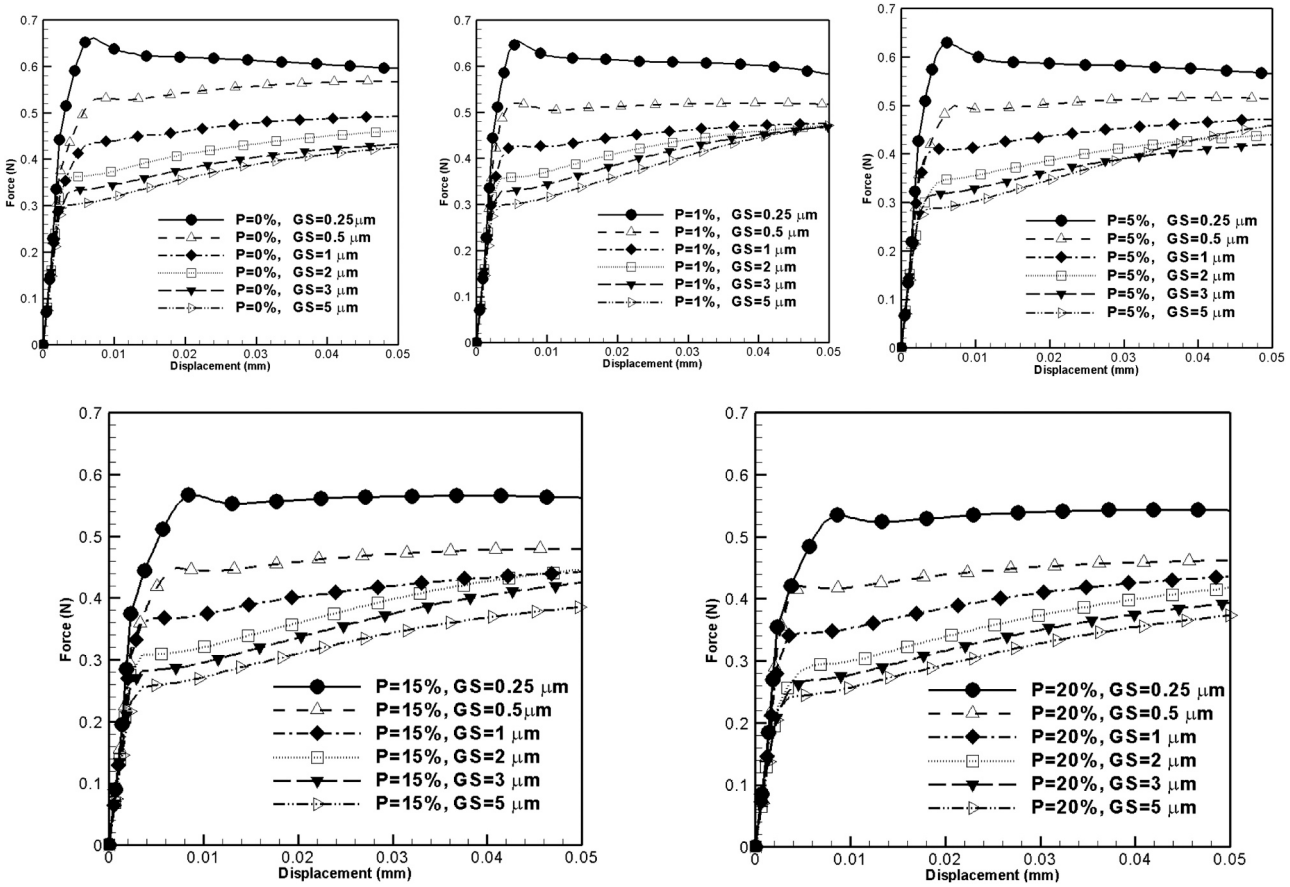


**Fig. 11.** Force vs. displacement for various porosity (P) and grain size (GS) values for case-II.

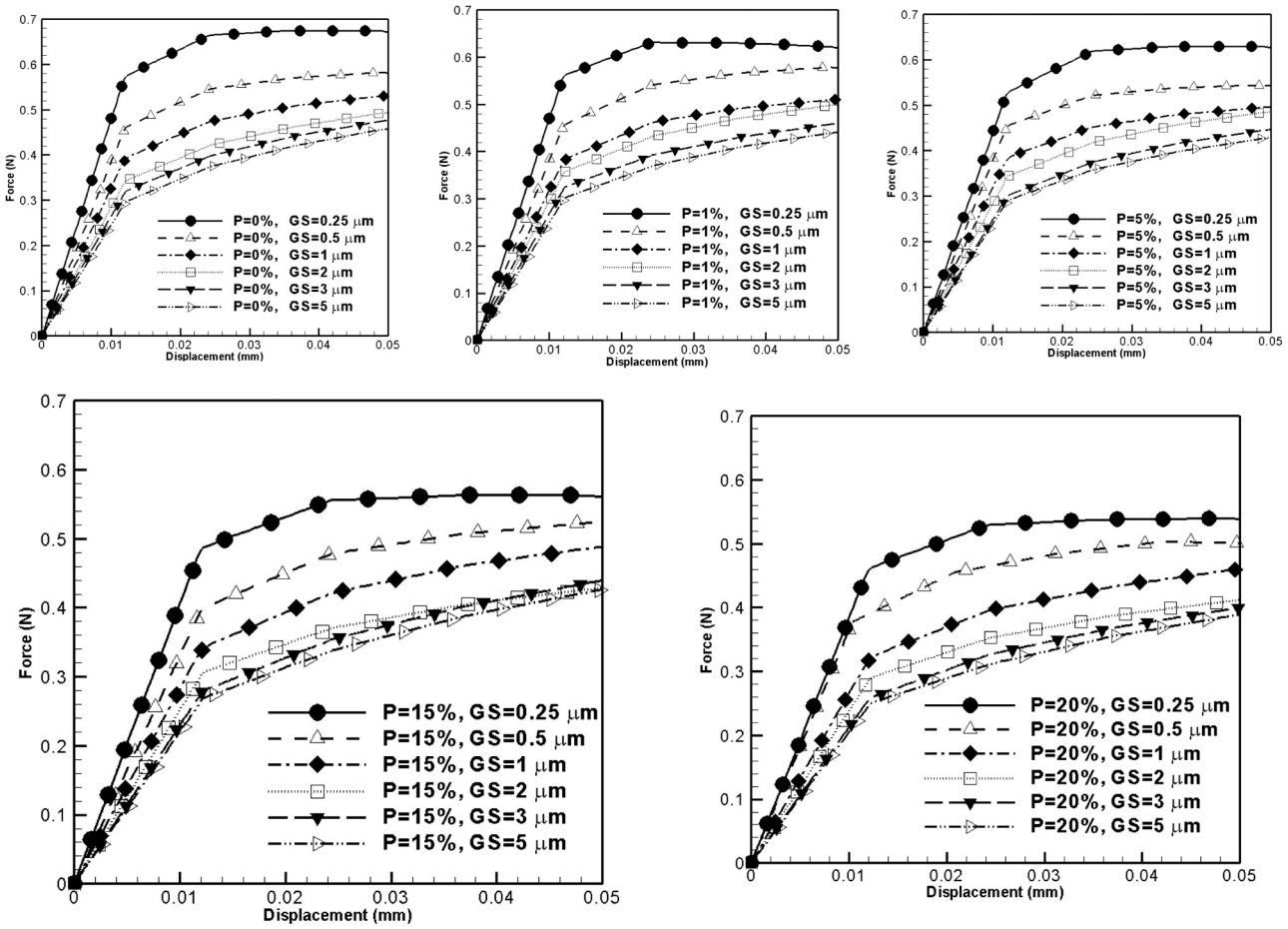


**Fig. 12.** Force vs. displacement for various porosity (P) and grain size (GS) values for case-III.

simulations were then performed using mesh2. In all these cases the initial dislocation density was set at $10^{13}/m^2$, which was selected based on the curve fitting discussed in the previous section.

The primary objective of these simulations was to investigate the interaction and trade-off between hardening resulting from size effects (grain refinement and gradients) and softening caused by porosity. We run a set of cases for porosities ranging from 0% to 20%, and grain sizes ranging from 250 nm to 5 μm. The results are summarized in Fig. 5. The figure shows force versus displacement of the upper surface of the micropillar. It can be deduced from the figure that the linear part of the curves is dependent upon the porosity as expected from Eq. (5); while the onset of yielding followed by buckling, depicted in Fig. 5, is dependent upon the grain size which is a result of the size dependent Eqs. (16) and (18). It is clear from Fig. 5 that the effect of grain size on the stress-strain relation is more dominant than the percentage porosity.

Typical deformed configurations and distribution of effective stress and effective plastic strain along the micropillar are shown in Fig. 6. As can be inferred from Fig. 6, in the buckled pillar, the plastic deformation and stress fields are non-uniform. The spatial gradients of these fields are continuously computed during the simulations to compute the GND and stress gradients appearing in Eqs. (16) and (17). Fig. 7a and b show the change of dislocation densities and GNDs with increased strain in an element at the center of the pillar. While the mobile and immobile dislocations begin to grow from the outset of plastic deformation, the GNDs begin to grow at the onset of buckling.

The initiation of buckling coincides with the first drop in the force as can be observed from Fig. 5. The maximum force where buckling initiates is extracted from these figures and the results are depicted in Figs. 8 and 9. Fig. 8 shows a family of curves corresponding to the various porosity densities, while Fig. 9 depicts a family of curves of force versus porosity for the various grain sizes. These results show that strengthening from grain refinement can be much stronger than softening caused by porosity. The result in Fig. 8 shows a power-law dependence of the buckling force $p$ on grain size $L$, while the result in Fig. 9 shows linear dependence on porosity $\phi$, suggesting a relationship of the form:

$$p \propto L^{-n}(1-\phi) \tag{19}$$

The dotted curves in Figs. 8 and 9 are fitted to the numerical results in the figure with $n = 0.227$. This value indicates a strong deviation from the classical Hall-Petch effect where typically $n = 0.5$. This deviation is attributed to gradient effects that enter in Eqs. (16) and (18). The deviation from the classic Hall-Petch is attributed to the presence of stress gradients and the specimen size of a few micrometers [17,20,21].

### 3.3. Micropillars with geometrical imperfections

As it is known, the AM processes give rise to a complex microstructure as well as manufacturing imperfections (e.g. Fig. 1) that need to be considered while modeling the mechanical behavior of the part. In this section, we analyze two additional micropillar geometries that account for imperfections. The micropillar geometry analyzed in Section 3.2 is referred to as case-I and the following cases in this part are referred to as case-II and case-III. Micropillars for case II, III are shown in Fig. 10 where the micropillar for case II has a reduced diameter at the bottom of the cylinder. For case-III, the micropillar has a reduced diameter at the bottom and is tilted about 5 degrees with respect to the vertical axis.

The same user material subroutine and formulation as case-I was applied for micropillars in case-II and case-III. The force vs displacement

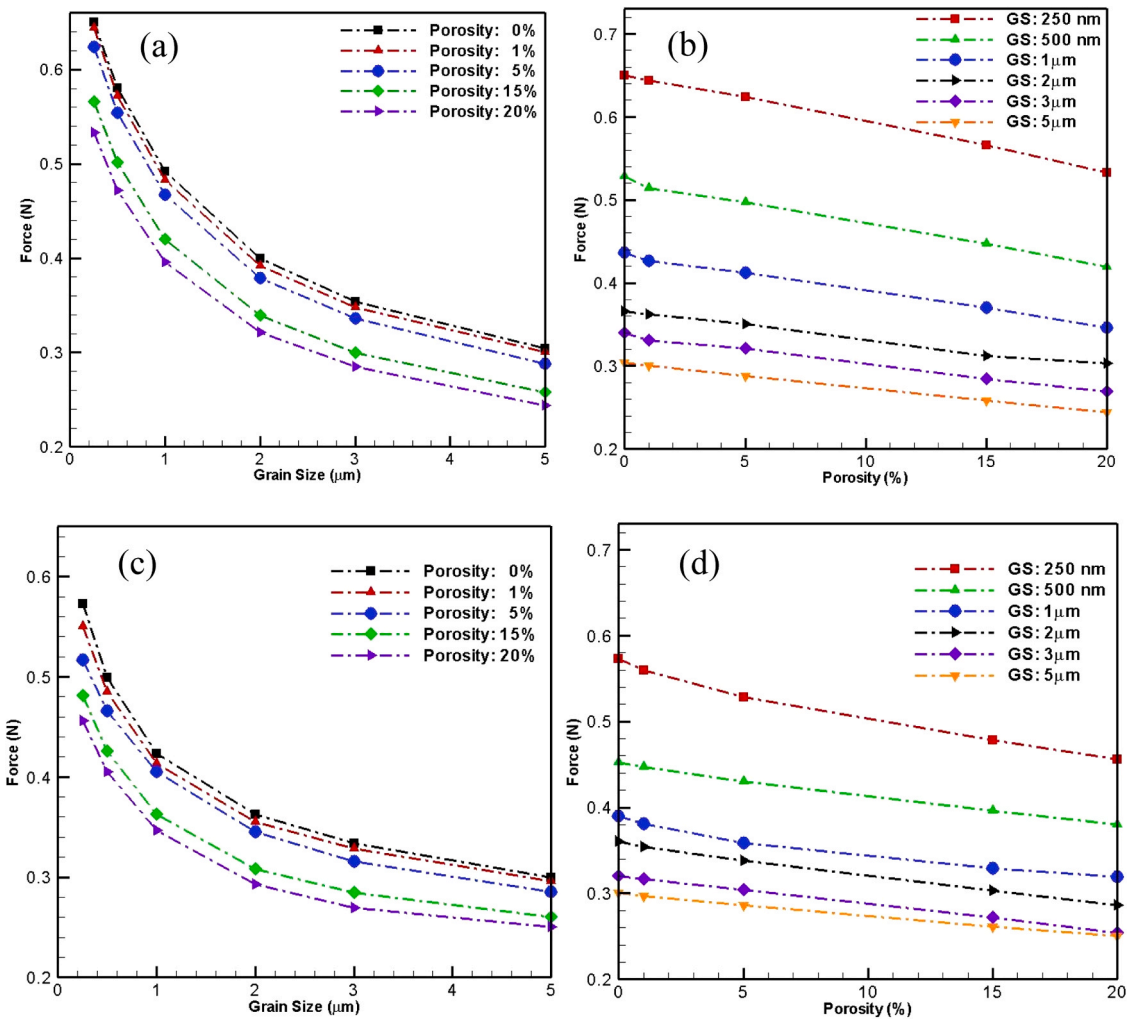


**Fig. 13.** Buckling force for micropillars with imperfections. (a) Force vs grain size (GS), and (b) force vs porosity for micropillars in case-II. (c) Force vs grain size, and (d) force vs porosity for micropillars in case-III.

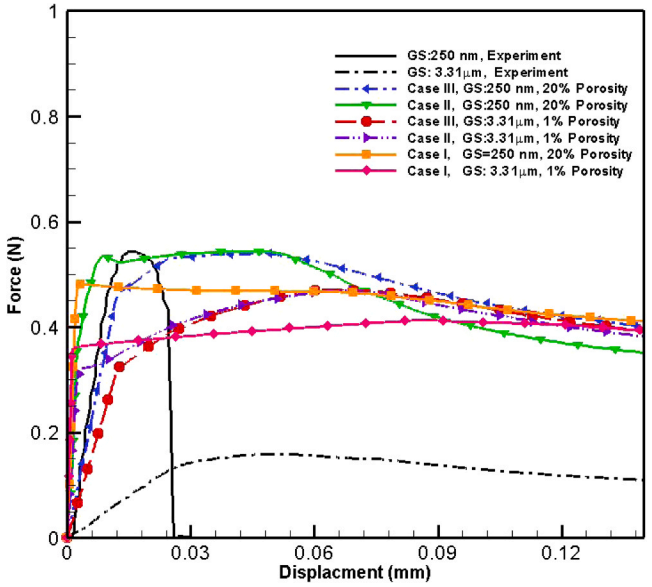


**Fig. 14.** A comparison between experimental and simulation results for force vs displacement graph at different grain size (GS) and porosity values.

for these new categories are shown in Fig. 11 and Fig. 12.

By comparing Figs. 11, 12, and Fig. 5, it is obvious that introducing geometrical imperfections to micropillars (case-II and case-III) leads to lowering the maximum force value while the deflection of pillars is increased by an order of magnitude. Further, comparing the slope of the curves after onset of buckling in the aforementioned figures shows the effect of localized hardening due to geometrical imperfections, which was absent in Fig. 5. The geometrical irregularities in these sets of micropillars cause a non-uniform distribution of stress intensity along the micropillars which leads to stress gradients which, in turn, and according to Eq. (18), causes additional hardening.

The variation of buckling forces for micropillars in case-II and case-III for different porosity and grain sizes are shown in Fig. 13 a–d.

The stress at which the onset of buckling occurs is the highest for micropillars with the smallest grain sizes and lowest porosity, while this value drops down for higher grain sizes and higher porosity. The onset of buckling forces for micropillars in all three categories show a stronger

**Table 3**
Force at the onset of buckling.

| Grain size | $P_{Buckling}$ (experiment) (N) | $P_{Buckling}$ (case I) (model) (N) | $P_{Buckling}$ (case II) (model) (N) | $P_{Buckling}$ (case III) (model) (N) |
|---|---|---|---|---|
| 250 nm | 0.54 | 0.48 | 0.533 | 0.456 |
| 3.31 μm | 0.14 | 0.37 | 0.293 | 0.25 |

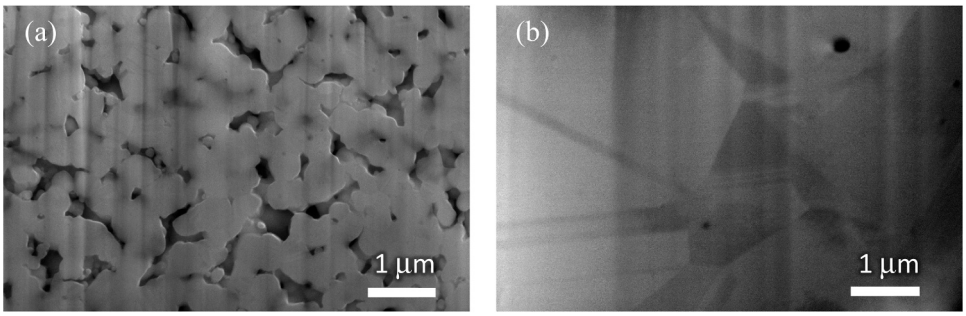


**Fig. 15.** FIB cross-section images showing distribution and average void size of micropillars (a) with 250 °C sintering temperature and average grain size of 250 nm, and (b) 550 °C sintering temperature and average grain size of 3.31 μm.

dependency on grain size changes rather than the porosity variation, especially for grain sizes below 1 micrometer. Further, a comparison of Fig. 13 with Figs. 8 and 9 shows that the presence of geometrical imperfections lowers the maximum buckling force for a given grain size and porosity.

## 4. Comparison with experiments and discussion

Fig. 14 shows a comparison of the modeling results with experiments in Saleh et al. [1]. Two sets of micropillars tested in compression are included in Fig. 14: One set of results for micropillars sintered at 250 °C and having 17–20% porosity with the void sizes of 250–300 nm, while another set of micropillars sintered at 550 °C and having less than 1% porosity with a pore size of 170 nm. According to the parametric findings discussed in the previous section, and summarized in Figs. 8, 9, and 13, it is expected that the micropillars sintered at 250 °C should be stronger than that sintered at 550 °C even though the latter have much less porosity than the former. These experimental trends are qualitatively comparable to the numerical findings as shown in Fig. 14. The experimental and numerical results for the maximum force are comparable for the case of micropillars with an average grain size of 250 nm where there is less than 5% difference between the predicted maximum force and experimental result (Table 3).

Although the model is able to capture the experimental trends qualitatively, it is clear that there is a quantitative difference between the two for the force-displacement curves. This is especially true for micropillars with an average grain size of 3.31 μm. We speculate that this difference comes from the fact that our model does not include damage and therefore the ultimate elongation cannot be matched with experimental data. Further, the pores and their facets can act as sources or sinks of dislocations, which has not been taken into account. It is clear from Fig. 2 that the dislocation density can significantly affect the predicted stress-strain response from this model. Further, higher sintering temperature in the case with an average grain size of 3.31 μm can increase the percentage of low-angle grain boundaries and dislocation density transfer amongst neighboring grains, which can lead to higher ductility and lower yield point [18,45,49]; where none of these phenomena are considered in our model. We would like to emphasize that the microstructures demonstrated in Fig. 1 are highly complex and the trends in the mechanical behavior captured by our model are reasonable. The disparities mentioned above, however, point to the fact that further refinements to the model can be incorporated.

Another noticeable difference between the modeling and the experimental results is that the experimental load for the micropillars with 250 nm grain size drops sharply after 0.025 mm deflection which represents catastrophic failure. Although in the modeling result, the load drop is visible for these micropillars, since no failure criterion is implemented into the model, the drop is not as catastrophic as that observed in the experiments. This difference can also be attributed to void sizes and distribution. The void sizes and distribution for the two experimental micropillars are shown in Fig. 15. Voids can act as stress concentrators where shear bands and cracks can initiate, which indicates that in addition to porosity percentage, the void size and distribution will also influence the pillar behavior. These results indicate that additively manufactured micropillars can possess high strength despite their high porosity content as long as their microstructure is composed of submicron-grains.

## 5. Conclusions

In this paper, a modeling framework that describes the mechanical behavior of AM parts is developed and used to explain prior experimental results by the authors in the context of a competition between softening caused by porosity and hardening caused by grain refinement. The following conclusions can be drawn from the study:

- A stress-strain gradient model where deformation is described via equations of dislocation density evolution is implemented into a UMAT subroutine and coupled with LS-DYNA solver to analyze the mechanical behavior of additively manufactured structures. This formulation incorporates the grain size and porosity of the structure via a viscoplasticity model, which is coupled with the continuum dislocation dynamics framework.
- The model reveals that the mechanical behavior of AM structures is governed by a competition between strengthening caused by grain refinement and softening caused by the porosity within the structures.
- The model was used to analyze experimentally observed compression behavior of AM micropillars previously studied by the authors, where three sets of geometries (with and without shape imperfections) were analyzed for grain sizes ranging from a few hundred nanometers to a few micrometers and porosities ranging from 0 to 20%.
- The model showed that the hardening caused by grain refinement was a stronger effect compared to softening caused by porosity. This led to structures with larger micron-sized grains with low porosity having a highly ductile behavior with lower effective modulus compared to those with sub-micron grains and high porosity. This unusual prediction was consistent with the experimental results on AM micropillars.
- The localized stress and strain originated due to shape imperfection were captured by the model. The existing shape imperfection caused early buckling and lowered the maximum buckling force for the AM micropillar structures considered in this work.

## CRediT authorship contribution statement

R.P. and H.Z. came up with the concept and directed the research. M. H. carried out the simulations and wrote the first draft of the paper. S.S. carried out the experimental part of the paper. A.A. helped with the simulations. All authors contributed to interpreting the data and preparing and editing the manuscript.

## Declaration of Competing Interest

The authors declare that they have no known competing financial interests or personal relationships that could have appeared to influence the work reported in this paper.

## Acknowledgement

This work was supported by the National Science Foundation under Grant No. 1757117.

## Appendix A. Supporting information

Supplementary data associated with this article can be found in the online version at doi:10.1016/j.addma.2020.101833.

## References

[1] M.Sadeq Saleh, M. HamidVishkasougheh, H. Zbib, R. Panat, Polycrystalline micropillars by a novel 3-D printing method and their behavior under compressive loads, Scr. Mater. 149 (2018) 144–149.
[2] D. Herzog, V. Seyda, E. Wycisk, C. Emmelmann, Additive manufacturing of metals, Acta Mater. 117 (2016) 371–392.
[3] I. Gibson, D.W. Rosen, B. Stucker, Additive Manufacturing Technologies, vol. 17, Springer, 2014.
[4] N.H. Paulson, B. Gould, S.J. Wolff, M. Stan, A.C. Greco, Correlations between thermal history and keyhole porosity in laser powder bed fusion, Addit. Manuf. 34 (2020), 101213.
[5] P.C. Collins, D.A. Brice, P. Samimi, I. Ghamarian, H.L. Fraser, Microstructural control of additively manufactured metallic materials, Annu. Rev. Mater. Res. 46 (2016) 63–91.
[6] M.S. Saleh, J. Li, J. Park, R. Panat, 3D printed hierarchically-porous microlattice electrode materials for exceptionally high specific capacity and areal capacity lithium ion batteries, Addit. Manuf. 23 (2018) 70–78.
[7] Y. Zhu, J. Li, M.S. Saleh, H. Pham, T.P. Plateau, R. Panat, J. Park, Towards high-performance Li-ion batteries via optimized three-dimensional micro-lattice electrode architectures, J. Power Sources 476 (2020), 228593.
[8] M.T. Rahman, J. McCloy, C.V. Ramana, R. Panat, Structure, electrical characteristics, and high-temperature stability of aerosol jet printed silver nanoparticle films, J. Appl. Phys. 120 (7) (2016), 075305.
[9] N.A. Fleck, G.M. Muller, M.F. Ashby, J.W. Hutchinson, Strain gradient plasticity: theory and experiment, Acta Metall. Mater. 42 (2) (1994) 475–487.
[10] N. Wang, Z. Wang, K.T. Aust, U. Erb, Effect of grain size on mechanical properties of nanocrystalline materials, Acta Metall. Mater. 43 (2) (1995) 519–528.
[11] Z. Fan, A. Miodownik, P. Tsakiropoulos, Microstructural characterisation of two phase materials, Mater. Sci. Technol. 9 (12) (1993) 1094–1100.
[12] Y.M. Wang, T. Voisin, J.T. McKeown, J. Ye, N.P. Calta, Z. Li, Z. Zeng, Y. Zhang, W. Chen, T.T. Roehling, R.T. Ott, M.K. Santala, P.J. Depond, M.J. Matthews, A. V. Hamza, T. Zhu, Additively manufactured hierarchical stainless steels with high strength and ductility, Nat. Mater. 17 (1) (2018) 63–71.
[13] M. Taheri Andani, M.R. Karamooz-Ravari, R. Mirzaeifar, J. Ni, Micromechanics modeling of metallic alloys 3D printed by selective laser melting, Mater. Des. 137 (2018) 204–213.
[14] A. Siddiq, A porous crystal plasticity constitutive model for ductile deformation and failure in porous single crystals, Int. J. Damage Mech. 28 (2) (2018) 233–248.
[15] D. Li, H. Zbib, X. Sun, M. Khaleel, Predicting plastic flow and irradiation hardening of iron single crystal with mechanism-based continuum dislocation dynamics, Int. J. Plast. 52 (2014) 3–17.
[16] H. Lyu, M. Hamid, A. Ruimi, H.M. Zbib, Stress/strain gradient plasticity model for size effects in heterogeneous nano-microstructures, Int. J. Plast. 97 (2017) 46–63.
[17] M. Hamid, H. Lyu, H. Zbib, A dislocation-based stress-strain gradient plasticity model for strength and ductility in materials with gradient microstructures, Philos. Mag. 98 (32) (2018) 2896–2916.
[18] M. Hamid, et al., Modeling and characterization of grain boundaries and slip transmission in dislocation density-based crystal plasticity, Crystals 7 (6) (2017) 152.
[19] H. Askari, J. Young, D. Field, G. Kridli, D. Li, H. Zbib, A study of the hot and cold deformation of twin-roll cast magnesium alloy AZ31, Philos. Mag. 94 (4) (2014) 381–403..
[20] N. Taheri-Nassaj, H.M. Zbib, On dislocation pileups and stress-gradient dependent plastic flow, Int. J. Plast. 74 (2015) 1–16.
[21] S. Akarapu, J. Hirth, Dislocation pile-ups in stress gradients revisited, Acta Mater. 61 (10) (2013) 3621–3629.
[22] S.S. Chakravarthy, W. Curtin, Stress-gradient plasticity, Proc. Natl. Acad. Sci. USA 108 (38) (2011) 15716–15720.
[23] T. Ohashi, M. Kawamukai, H. Zbib, A multiscale approach for modeling scale-dependent yield stress in polycrystalline metals, Int. J. Plast. 23 (5) (2007) 897–914.
[24] K. Shizawa, H.M. Zbib, A strain-gradient thermodynamic theory of plasticity based on dislocation density and incompatibility tensor, Mater. Sci. Eng. A (2000).
[25] T. Ohashi, Crystal plasticity analysis of dislocation emission from micro voids, Int. J. Plast. 21 (11) (2005) 2071–2088.
[26] Livemore Software Technology Corporation, Software Products and Documentation, 2011. Available from: ⟨http://www.lstc.com/download⟩.
[27] C.N. Tome, R.A. Lebensohn, Manual for code Visco Plastic Self Consistent (VPSC), 2009.
[28] W. Xu, X. Sun, B.J. Koeppel, H.M. Zbib, A continuum thermo-inelastic model for damage and healing in self-healing glass materials, Int. J. Plast. 62 (2014) 1–16.
[29] P. Perzyna, Constitutive modeling of dissipative solids for postcritical behavior and fracture, Trans. ASME 106 (1984) 410–419.
[30] M. Khaleel, H.M. Zbib, E.A. Nyberg, Constitutive modeling of deformation and damage in superplastic materials, Int. J. Plast. 17 (2001) 277–296.
[31] E. Orowan, Problems of plastic gliding, Proc. Phys. Soc. 52 (1) (1940) 8–22.
[32] M. Khaleel, H. Zbib, E. Nyberg, Constitutive modeling of deformation and damage in superplastic materials, Int. J. Plast. 17 (3) (2001) 277–296.
[33] D. Steglich, H. Wafai, J. Besson, Interaction between anisotropic plastic deformation and damage evolution in Al 2198 sheet metal, Eng. Fract. Mech. 77 (17) (2010) 3501–3518.
[34] U.F. Kocks, Laws for work-hardening and low-temperature creep, ASME Trans. Ser. H J. Eng. Mater. Technol. 98 (1976) 76–85.
[35] J.E. Bailey, P.B. Hirsch, The dislocation distribution, flow stress, and stored energy in cold-worked polycrystalline silver, Philos. Mag. 5 (53) (1960) 485–497.
[36] J. Nye, Some geometrical relations in dislocated crystals, Acta Metall. 1 (2) (1953) 153–162.
[37] K. Shizawa, H. Zbib, A thermodynamical theory of gradient elastoplasticity with dislocation density tensor. I: Fundamentals, Int. J. Plast. 15 (9) (1999) 899–938.
[38] T. Ohashi, Finite-element analysis of plastic slip and evolution of geometrically necessary dislocations in fcc crystals, Philos. Mag. Lett. 75 (2) (1997) 51–58.
[39] (LSTC), L.S.T.C., LS DYNA keyword user's manual. 2013.
[40] B. Wu, A. Heidelberg, J.J. Boland, J.E. Sader, Sun, Li, Microstructure-hardened silver nanowires, Nano Lett. 6 (3) (2006) 468–472.
[41] Matweb, ⟨http://www.matweb.com⟩.
[42] D.R. Smith, F.R. Fickett, Low temperature properties of silver, J. Res. Natl. Inst. Stand. Technol. 100 (1995) 119.
[43] Y. Li, A.J. Bushby, D.J. Dunstan, The Hall–Petch effect as a manifestation of the general size effect, Proc. R. Soc. A Math. Phys. Eng. Sci. 472 (2190) (2016), 20150890.
[44] G. Schoeck, W. Püschl, The kink energy in anisotropic media, Phys. Status Solidi (b) 144 (1) (1987) 105–114.
[45] M. Hamid, H.M. Zbib, Dislocation density-based multiscale modeling of deformation and subgrain texture in polycrystals, JOM 71 (11) (2019) 4136–4143.
[46] M. Dao, L. Lu, Y.F. Shen, S. Suresh, Strength, strain-rate sensitivity and ductility of copper with nanoscale twins, Acta Mater. 54 (2006) 5421–5432.
[47] X. Long, W. Tang, Y. Feng, C. Chang, L.M. Keer, Y. Yao, Strain rate-sensitivity of sintered silver nanoparticles using rate-jump indenation, Int. J. Mech. Sci. 140 (2018) 60–67.
[48] K.J.H. Al-Fadhalah, C.M. Li, A.J. Beaudoin, D.A. Korzekwa, I.M. Robertson, Microplastic processes developed in pure Ag with mesoscale annealing twins, Acta Mater. 56 (19) (2008) 5764–5774.
[49] M. Jamalian, M. Hamid, N. De Vincentis, Q. Buck, D.P. Field, H.M. Zbib, Creation of heterogeneous microstructures in copper using high-pressure torsion to enhance mechanical properties, Mater. Sci. Eng. A 756 (2019) 142–148.